



# Functional repair of critically sized femoral defects treated with bioinspired titanium gyroid-sheet scaffolds

Cambre N. Kelly<sup>a,b</sup>, Angela SP. Lin<sup>c</sup>, Kelly EH. Leguineche<sup>c</sup>, Sudhanshu Shekhar<sup>c</sup>, William R. Walsh<sup>d</sup>, Robert E. Guldberg<sup>c</sup>, Ken Gall<sup>a,b,\*</sup>

<sup>a</sup> Department of Biomedical Engineering, Duke University, Durham, NC, USA

<sup>b</sup> Department of Mechanical Engineering and Materials Science, Duke University, Durham, NC, USA

<sup>c</sup> The Knight Campus for Accelerating Scientific Impact, University of Oregon, Eugene, OR, USA

<sup>d</sup> Surgical and Orthopedic Research Laboratories, University of New South Wales, Sydney, New South Wales, Australia

## ARTICLE INFO

### Keywords:

Critically sized bone defect  
Scaffold  
Gyroid  
Osseointegration

## ABSTRACT

Despite the innate ability for bone to remodel and repair, its regeneration has a limit. In these cases of critically sized bone defects (CSBD), the bone deficit must be repaired using reconstructive techniques that support immediate load bearing and encourage bone bridging across the defect. High-strength porous titanium implants offer a solution for treatment of CSBD in which the scaffold can support physiological loads, provide a matrix to guide ingrowth, and carry graft materials and/or biologics. Fabrication of titanium meta-materials via additive manufacturing (AM) has unlocked the potential to modulate mechanical and biological performance to achieve a combination of properties previously unachievable. Meta-material scaffolds with topology based on triply periodic minimal surfaces (TPMS) have gained increasing interest for use in biomedical applications due to their bioinspired nature. Despite enthusiasm for TPMS-based titanium scaffolds due to their high strength to stiffness ratio, high permeability, and curvature similar to trabecular bone, there is little preclinical evidence to support their in vivo response in bone. The present study sought to evaluate the performance of gyroid-sheet titanium scaffolds produced via AM to repair a critically size femoral cortical bone defect in rats. Empty gyroid-sheet scaffolds were shown to repair segmental defects with up to 38% of torsional strength and 54% torsional stiffness of the intact femur (control) at 12-weeks. Gyroid-sheet scaffolds carrying recombinant bone morphogenic protein-2 demonstrated bridging bone growth across the length of the defect, with torsional strength and stiffness superior to that of the intact controls.

## 1. Introduction

Critical-sized bone defects (CSBD) are defined as those which will not heal spontaneously, and typically are considered to be defects larger than two times the diameter of the long bone diaphysis (Roddy et al., 2018; Reichert et al., 2009; Schemitsch, 2017). In many cases of trauma, or resection due to malignant, infected or poor quality bone tissue, CSBD present a difficult challenge for reconstruction (Schemitsch, 2017; Dekker et al., 2018; Hamid et al., 2016). These defects must be restored by reconstructing the defect with a scaffold capable of supporting functional load bearing, as well as promoting a healing response at the appositional bone leading to a stable bone-implant interface, and subsequent healing.

Laser powder bed fusion (L-PBF), an additive manufacturing (AM)

method, has enabled creation of complex titanium scaffolds capable of supporting high loads and porosity for bone ingrowth. The spatial resolution and control of L-PBF has unlocked the ability to create scaffolds with complex topologies which were previously unachievable with traditional manufacturing methods. With additive manufacturing, a new paradigm of engineering has emerged with the capabilities to now create “meta-materials” at the mesoscale and macroscale which can be designed and fabricated to have prescribed topological, mechanical, and biological properties that cannot be achieved in their solid counterpart. As discussed by Zadpoor and others, meta-materials can be considered as composites, where the distribution of the materials in a matrix gives varied properties at the macroscale (Zadpoor, 2015, 2017). The topology of a repeating unit cell defines the distribution of scaffold material, in this study titanium, in the matrix of void space (Zadpoor, 2018).

\* Corresponding author. Department of Biomedical Engineering, Duke University, Durham, NC, USA.

E-mail address: [ken.gall@duke.edu](mailto:ken.gall@duke.edu) (K. Gall).

<https://doi.org/10.1016/j.jmbbm.2021.104380>

Received 16 November 2020; Received in revised form 5 January 2021; Accepted 30 January 2021

Available online 4 February 2021

1751-6161/© 2021 The Authors.

Published by Elsevier Ltd.

This is an open access article under the CC BY-NC-ND license

(<http://creativecommons.org/licenses/by-nc-nd/4.0/>).

However, unlike composites, meta-materials can possess properties outside of the range of either constituent phase. For bone tissue engineering, this means modulation of strength and stiffness, as well as control over porosity, permeability, surface area, and pore size to create bone-mimicking scaffolds with improved osseointegration potential. Further, the interconnected void space with high surface area can be filled with a second material to make a true composite and alter the mechanical or biological properties of the scaffold for the desired applications. Metallic scaffolds which provide mechanical support can be filled with degradable bioceramics or polymers for delivery of growth factors or drugs (Zadpoor, 2018; van der Stok et al., 2013). Similarly, in clinical practice, porous metallic implants used in attainment of union of the lower extremities are often filled with autogenic, allogenic, or synthetic bone graft to promote bony fusion (Walsh et al., 2019; Yuan et al., 2010; Habibovic and de Groot, 2007; Dimitriou et al., 2011). Recent work has shown the implantation site in a preclinical model does significantly influence bone ingrowth in 3D porous implants, along with graft material, surgical technique, and loading biomechanics (Walsh et al., 2019). Preclinical models for evaluation of treatments for cortical CSBD include small (rat, rabbit) and large animal (canine, sheep). The variety of species, surgical technique, treatment, fixation method, time points, and evaluation assays make direct comparison from model to model difficult (Reichert et al., 2009). Previously reported preclinical models evaluating the osseointegration potential of porous titanium produced via traditional or additive manufacturing method are summarized in Table 1.

Triply periodic minimal surfaces (TPMS) have gained interest for design of meta-materials for biomedical and other applications. TPMS unit cells include gyroid, primitive, and diamond, which are defined by sinusoidal functions and characterized by their zero mean curvature (Karcher, 1989). The cubic symmetry of gyroid and other TPMS structures results in fully interconnected porous networks with high surface area. Natural occurrence of gyroid structures have been observed on the nanoscale in the wings of butterflies and intercellular membranes. Gyroid topologies have been mimicked in nanofabrication of block co-polymers and photonic crystals (Wiltz et al., 2017). Although the natural existence and mathematical basis of minimal surfaces has been studied for over five decades (Karcher, 1989), fabrication of bioinspired TPMS topologies at the meso/macroscale was not realized until the development of advanced additive manufacturing technologies. In addition to heat transfer and energy absorption applications, TPMS unit cells have been proposed for biomedical applications (Zadpoor, 2015; Bobbert et al., 2017; Kelly et al., 2019a; Yu et al., 2020). Driven by recent evidence that the role of substrate curvature is important in tissue regeneration, TPMS-based meta-materials have received greatly increased interest for use as tissue engineering scaffolds as they have been shown to have local curvature similar to trabecular bone (Zadpoor, 2015; Bobbert et al., 2017). The growing interest in TPMS-based meta materials has produced characterization of the control over mechanical properties, particularly elastic-modulus and strength, driven by topology. Topology of TPMS-based scaffolds is defined by their type, unit cell, and porosity. Type can be either cellular (skeletal) or sheet-based, which

can be designed by enclosing the volume contained by or thickening the minimal surface, respectively. Unit cell is based on the periodic function defining the minimal surface which defines the cell type (gyroid, diamond, primitive, etc.) and the cell size. For scaffolds designed and fabricated by AM, typical cubic unit cell side lengths are 1–8 mm. Porosity (or void volume fraction) defines the ratio of material to void space and is controlled by modulation of the thickness of the struts (cellular) or walls (sheet-based). Porosity of scaffolds is within the porosity range of trabecular bone (50–90%) (Wall and Board, 2014). Pore size of the scaffold is dictated by the combination of scaffold type, unit cell, and porosity.

The growing interest in TPMS-based metamaterials for biomedical applications has resulted in many studies focused on the mechanical behavior and permeability (Bobbert et al., 2017; Ma et al., 2019; Al-Ketan et al., 2018; Mahmoud and Elbestawi, 2018). TPMS-based scaffolds can be designed with modulus in the range of trabecular and cortical bone and (Bobbert et al., 2017; Kelly et al., 2019a; Al-Ketan et al., 2018; Mahmoud and Elbestawi, 2018) have compressive strength, energy absorption, and fatigue resistance which exceeds that of strut-based scaffolds of the same porosity (Kelly et al., 2019a; Al-Ketan et al., 2018). The recent topological characterization and mechanical results for TPMS-based scaffolds suggests opportunity for superior osseointegrative performance. Despite broad mention of the hypothesized benefits of sheet based TPMS scaffolds due to the increased surface area and high permeability, little preclinical evidence exists for such scaffolds in an unconfined critically sized bone defect.

Performance of titanium scaffolds with various porous topologies have been studied in constrained cancellous and cortical bone defects (Walsh et al., 2019; Cheng et al., 2017), as well as more specialized preclinical models such as spinal interbody fusion (Walsh et al., 2019; Cheng et al., 2014, 2017; Li et al., 2019). However, these models do not mimic the loading profile seen in lower extremity CSBD and many solely report semi-quantitative imaging and histological results (Anne-Marie Pobloth et al., 2018). Due to the artifact caused by metal implants, a quantitative biomechanical endpoint which assesses the strength of the bone-implant interface is critical. In this study, the effect of pore size of gyroid-sheet scaffolds for treatment of a CSBD was assessed in an established critically sized rat femoral segmental defect (Kolambkar et al., 2011; Oest et al., 2007). Scaffolds were produced via L-PBF of titanium alloy (Ti6Al4V) with porosity of 70%, and small ( $3 \times 3 \times 3$  mm) or large ( $6 \times 6 \times 6$  mm) unit cells, resulting in scaffolds with small and large pores, respectively. Additionally, recombinant bone morphogenic protein-2 (BMP2) was delivered in an alginate hydrogel with a concentration of  $0.5 \text{ mg/cm}^3$  to assess the efficacy of the gyroid-sheet scaffold as a carrier for osteoinductive biologics (Fig. 1). Assessment of the biological performance included radiographic examination (X-ray and  $\mu\text{CT}$  imaging) throughout the 12-week implantation period, as well as ex vivo biomechanical and histological analysis.

**Table 1**

Critically sized cortical bone defect models evaluating titanium scaffold performance. NR = not reported, L-PBF = laser powder bed fusion, EBM = electron beam melting. Quotations reflect how the material was reported.

Ref.	Model		Scaffold		Porosity	Average Pore size
	Animal Model	Fixation	Material	Lattice		
Murakami et al. (2002)	Rabbit humeri	Intermedullary nail	CP titanium	Mesh	50%	350 $\mu\text{m}$
Anne-Marie Pobloth et al. (2018)	Sheep tibia	Fixation plate	"Titanium"	Honeycomb-like mesh produced via L-PBF	NR	NR
Lindsey et al. (2006)	Canine femur	Intermedullary nail	"Titanium"	Mesh walled cylinder	NR	NR
Li et al. (2016)	Goat metatarsus	Fixation plate	Ti6A4V	Diamond via EBM	33%	490 $\mu\text{m}$
Van der Stok et al. (2013)	Rat femur	Fixation plate	Ti6A4V	Dodecahedron via L-PBF	68 and 88%	120, 230 $\mu\text{m}$
van der Stok et al. (2013)	Rat femur	Fixation plate	Ti6A4V	Dodecahedron via L-PBF	88%	490 $\mu\text{m}$
Present	Rat femur	Fixation plate	Ti6A4V	Gyroid-sheet via L-PBF	70%	740, 1100 $\mu\text{m}$

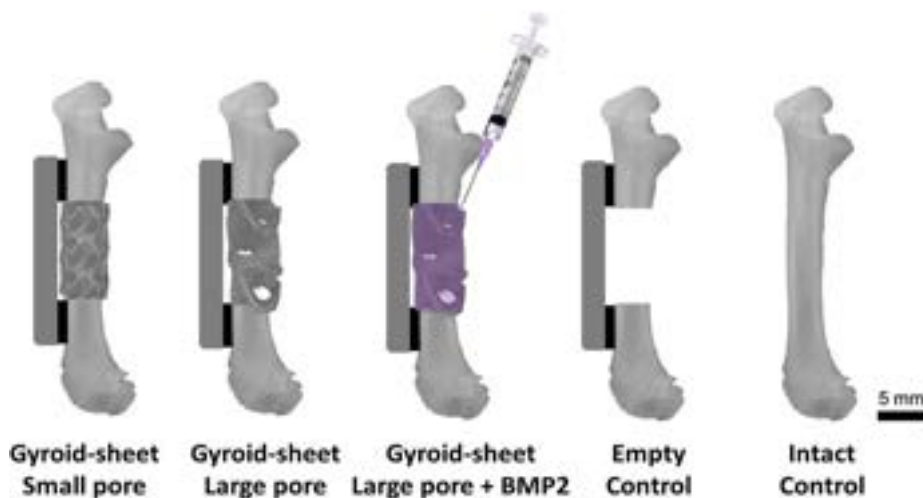


**Fig. 1.** Gyroid-sheet scaffolds with varied topology, and as a carrier for BMP2 were compared to empty defect and intact femur controls.

## 2. Methods

### 2.1. Scaffold fabrication and characterization

Scaffold implants with 4.5 mm diameter and 8 mm length were designed based on gyroid-sheet topology, to have large or small pore size (Fig. 2). Pore size was controlled by altering unit cell size, and wall thickness was adjusted to maintain the target relative porosity of 70%. Scaffolds were fabricated by L-PBF (3D Systems DMP ProX 320) with medical grade Titanium Alloy (Ti6Al4V ELI) powder. Using L-PBF, the

parts are created by deposition of a thin layer of powder, followed by scanning of the laser based on 2D slices of the 3D model, resulting in melting of the powder to coalesce and form a solid cross section of the desired part. This process is repeated layer by layer to build up the 3D part. L-PBF was conducted in an inert argon atmosphere to avoid oxidation of the titanium. Following printing, implants were hot isostatically pressed (HIP) per ASTM F3001 to reduce residual stresses and improve ductility. Implants were removed from the build plate by wire electric discharge machining, micro-blasted, and cleaned in a series of sonication steps. Steam sterilization of implants occurred on site prior

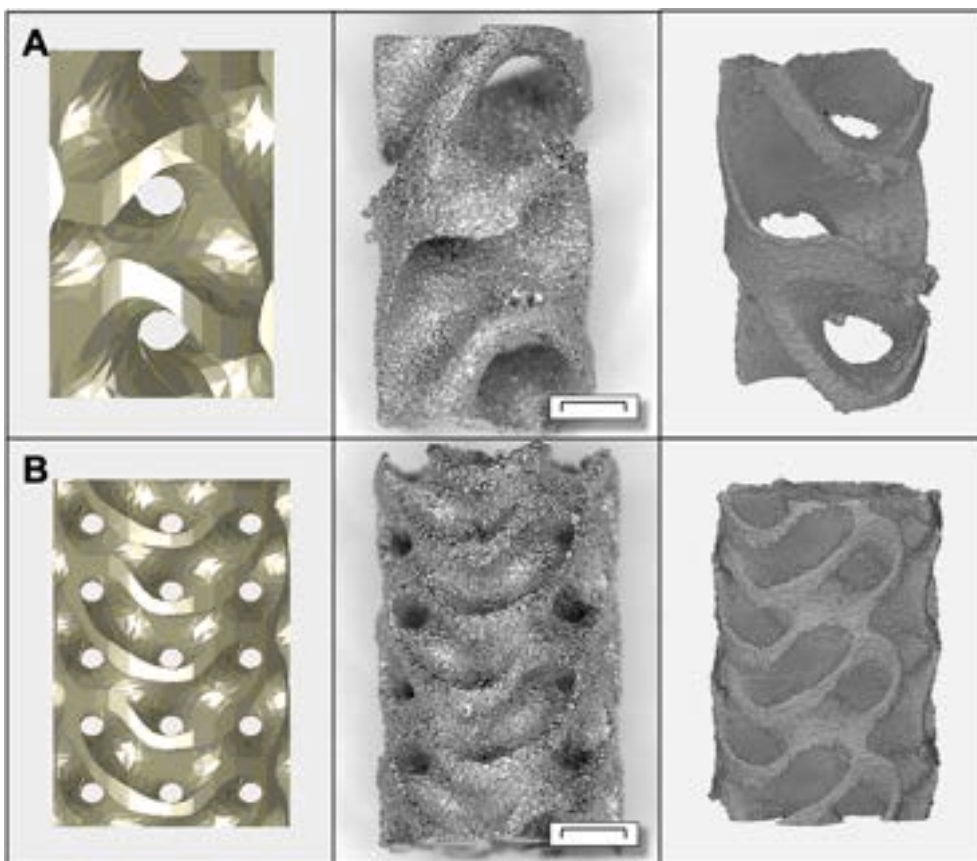


**Fig. 2.** CAD renderings, images of scaffolds, and  $\mu$ CT reconstructions of (A) large and (B) small pore gyroid-sheet scaffolds were additively manufactured by L-PBF of Ti6Al4V ELI. Scale bars are 1 mm.

to surgery.

$\mu$ CT was used to assess the porosity and morphology of some of the scaffold implants prior to surgery. Scaffold implants were scanned at 140 kV and 18 W at  $8 \mu\text{m}^3$  voxel size. Image reconstructions were made using CT Pro 3D software (Nikon) and volumetric renderings were created using Avizo software (FEI) to evaluate the printed implants compared to the CAD model. Image auto-thresholding was applied to distinguish material from void space, and then arithmetic operations were performed to calculate scaffold porosity. Analysis of pore size and wall thickness of the gyroid-sheet scaffolds was conducted using ImageJ (NIH) and the BoneJ plugin, using the methods described in detail by Bobbert (Bobbert et al., 2017).

## 2.2. Surgical procedure

All procedures were approved by the University of Oregon Institutional Animal Care and Use Committee and conducted in accordance to NIH Guide for Care and Use of Laboratory Animals. After arrival, rats were acclimated in single housing for 1–2 weeks with accessible unlimited food and water, and a 12/12-h light/dark cycle throughout the study. Surgery was conducted bilaterally on twenty six 13-week old female CD Sprague Dawley rats (Charles River) weighing approximately 250–300–400 g under isoflurane gas anesthesia (1.5–2.5%) using a previously established surgical procedure to provide internal stabilization with a fixation plate assembly prior to creating a bone defect (Oest et al., 2007; Cheng et al., 2019). In short, an anterolateral skin incision on the thigh and blunt dissection were performed to separate the overlying muscles to reach the femur. Surface of the femur was prepared to provide an unobstructed surface for fixation plate assembly placement. A custom-made radiolucent polysulfone fixation plate assembled intra-operatively with stainless steel risers was aligned and clamped in position, and holes were predrilled for securing the plate assembly to the femur using four 00–90 screws. A critically sized 8 mm defect was created in the mid-diaphysis of the femur using an oscillating saw (Hall Surgical Micro 100, Conmed Linvatec), and a scaffold implant was press fit into the defect (Fig. 1) followed by closure with muscle sutures (4-0 Vicryl) and 9 mm wound clips (Stoelting). A subcutaneous injection of sustained-release buprenorphine (approx. 0.65–1.5 mg/kg, ZooPharm) was administered for analgesia prior to surgery. For the large pore and BMP2 group, approximately  $5 \mu\text{g}$  of rhBMP2 was delivered in 100  $\mu\text{l}$  of alginate hydrogel injected into the scaffolds via sterile syringe and 20-gauge dispensing needle just prior to implantation in the defect. Details on preparation and release kinetics of the BMP2 alginate hydrogel are described in previous work (Kolambkar et al., 2011). Prior to surgery, benchtop testing was conducted to refine the methods for injection of the BMP alginate hydrogel into the implants. Repeatable injection volumes into large pore implants were achieved, however homogeneous injection of the hydrogel into the small pore implants proved difficult to achieve due to the tighter pore network, thus only large pore scaffolds were loaded with BMP2 for the study. At 12 weeks post-surgery, all animals were euthanized via  $\text{CO}_2$  inhalation, and both femora were harvested. Three animals ( $n = 3$  small pore scaffold defects,  $n = 3$  large pore scaffold + BMP2 defects), were euthanized within 1 week following surgery due to complications involving extensive tissue irritations around incision closures. All other animals healed the incisions, showed no adverse reactions, and were observed to be ambulating and weight bearing at normal activity levels.

## 2.3. In Vivo and ex vivo imaging

Implant alignment and longitudinal bone growth were observed via radiography (Faxitron UltraFocus, Faxitron X-ray Corp, Tucson, AZ) taken at 2, 4, 6, 8, and 12 weeks. *Ex vivo*  $\mu$ CT (vivaCT 80, Scanco Medical, Brüttisellen, Switzerland) was conducted on the harvested femurs at 12 weeks with a voxel size of  $36 \mu\text{m}$ . Harvested femora from each animal were each placed in saline-saturated gauze in 15 ml conical

tubes, and the two conical tubes placed side-by-side in a scan holder to scan both defect regions at once within a smaller field of view compared to the *in vivo* scans. Scan and reconstruction settings: E = 70 kVp, I = 114  $\mu\text{A}$ , integration time = 500 ms, pixel matrix  $1024 \times 1024$ .

Bone volumes measured from  $\mu$ CT reconstructions of the explanted femurs were assessed as total bone growth, bone ingrowth, normalized bone ingrowth, and normalized interface ingrowth. The total bone growth was assessed between the proximal and distal native bone ends of the defect, with no outer radial boundaries. Bone ingrowth volume was defined as the bone volume within a cylindrical volume of interest (VOI) with a diameter of 5.0 mm aligned with the inertial axis of the implant volume and between the native bone ends. Normalized bone ingrowth was calculated by dividing bone ingrowth by the available pore volume within the VOI. Bone ingrowth at each interface was assessed by calculating the bone volume within a cylindrical VOI with 5.0 mm diameter and 0.5 mm height at the most proximal or distal ends of implant. Normalized interface ingrowth values reported are divided by the available pore volume with the VOI for the bone end which had less bone (weaker bone end).

## 2.4. Biomechanical assessment

Torsional testing was used to assess the strength at the implant-bone interface. Harvested femurs were potted in custom fixtures with Woods metal (Belmont Metals, New York, USA) to secure and stabilize the proximal and distal ends and maintain appropriate anatomical alignment and gauge length. Fixtures were mounted to grips on a TA Instruments Electroforce 3220 axial torsion frame, using a 2 N-m load cell. Femurs were tested at constant rotation of  $3^\circ/\text{second}$  to  $100^\circ$  of total rotation. Torque-rotation plots were used to assess maximum torque and torsional stiffness, defined as the slope of the curve in the initial linear region. The maximum torque reported was the first maximum observed as this represents functional failure of the bone-implant interface. Following torsion testing, all tested femurs were fixed in 10% neutral buffered formalin (NBF) for histology processing.

## 2.5. Histological preparation and analysis

Following dehydration in ethanol and embedding in PMMA using established hard tissue histology techniques, defects were sectioned along the long axis of the implant (Leica SP 1600 Microtome) with a minimum of 2 levels (thin sections of  $\sim 15 \mu\text{m}$ ) taken from each implant. Each section was etched in acidic ethanol and stained with methylene blue followed by basic fuchsin (Walsh et al., 2019; Yuan et al., 2010). The resulting stain renders bone in pink and fibrous tissue in purple/blue. Sections were reviewed using microscopy, including low magnification overviews and high magnification observation of sites of interest, including the bone-implant interfaces and local bone response.

## 2.6. Statistical analysis

For biomechanical results, Kruskal-Wallis with Dunn's multiple comparisons test was used to compare bone formation metrics, as well as torsional strength and stiffness between all groups represented. Defects in which the implant was observed on the 12-week radiograph to have a significantly misaligned implant ( $n = 3$ ) or fracture to the proximal femur ( $n = 2$ ) were excluded from statistical analysis.

# 3. Results

## 3.1. Scaffold characterization

Comparison of printed scaffold topology to the CAD models revealed slight deviations in topology (Table 2). Scaffold porosity was found to be less than the designed CAD model for the small pore implants, likely due to the higher surface area relative to the large pore implants. Reduction



**Table 2**

Topological characterization of gyroid-sheet scaffolds. Design parameters for the CAD models compared to the  $\mu$ CT evaluation of the titanium scaffolds produced via L-PBF.

Implant	Defined in CAD Model				$\mu$ CT Evaluation		
	CAD Porosity (%)	Unit Cell Size (mm)	Sheet thickness ( $\mu$ m)	CAD Surface Area ( $\text{mm}^2$ )	Porosity (%)	Pore Size ( $\mu$ m)	Sheet thickness ( $\mu$ m)
Large Pore	70	6	600	147	70.8 (0.4)	1076 (135)	568 (27)
Small Pore	70	3	300	258	62.8 (0.5)	739 (47)	388 (34)

**Table 3**

Biomechanical results from ex vivo torsion tests of segmental defects treated with titanium scaffolds with and without additional growth factors. Stiffness and maximum torque are reported as normalized to the intact bone controls in each study. CaP = calcium phosphate, BMP2 = bone morphogenic protein 2, Fb = fibrin, NR = not reported.

Reference	Animal Model	Treatment	Endpoint (weeks)	Normalized Stiffness	Normalized Max Torque
Wieding et al. (2015)	Sheep Metatarsus	Scaffold +CaP coating	12	99%	30%
Lindsey et al. (2006)	Goat Metatarsus	Empty Scaffold	18	46%	NR
van der Stok et al. (2015)	Rat Femora	Empty Scaffold	12	NR	53%
van der Stok et al. (2015)	Rat Femora	Scaffold +BMP2/Fb	12	NR	248%
Van Der Stok et al. (2015)	Rat Femora	Scaffold +Osteostatin coating	12	NR	66%
Present	Rat Femora	Empty Scaffold	12	54%	38%
Present	Rat Femora	Scaffold +BMP2	12	244%	120%

in porosity of up to 10% is common in L-PBF parts due to adherence of partially adhered particles to the surface of the scaffolds during the fabrication process (Kelly et al., 2019a). The average pore size of the large pore implant was 1076  $\mu$ m, while the small pores were on average 739  $\mu$ m (see Table 3).

### 3.2. Imaging evaluation

X-ray radiographs were taken at intervals throughout the study and showed early bone formation around bone-implant interfaces by 4 weeks, with the most notable growth seen in the defects treated with large pore scaffolds with BMP2. Radiographic assessment of ingrowth into the implants was obscured by the metal artifact of the titanium. However, defects treated with BMP2 exhibited longitudinal growth around the implant that was clear on radiographs as early as 4 weeks (S. I. Fig. 1). Conversely, none of the empty defects demonstrated bone bridging at 12-weeks confirming that the defects were indeed critically sized (Fig. 3D).

Measurement of bone volumes via ex vivo  $\mu$ CT at 12 weeks were used to assess total bone growth and bone ingrowth within the metal scaffolds. The BMP2 group exhibited the highest total bone growth and bone ingrowth within the defined VOI (Fig. 4). Total bone growth and bone ingrowth within the VOI were significantly less for both small and large pore scaffolds versus the large pore scaffold with BMP2. However, while empty large pore implants exhibited significantly lower ingrowth at the

interface compared to those BMP2 group ( $p = 0.04$ ), there was no difference between normalized interface ingrowth between small pore and large pore + BMP2 implants ( $p = 0.13$ ).

### 3.3. Biomechanical assessment

Torque-rotation plots showed an initial linear region up to a peak torque, typically followed by a load drop associated with failure of the bone-implant interface, or in the cortical layer of the intact femora (as well as one defect treated with BMP2 which exhibited failure distal to the bone-implant interface). For several defects, a second peak was observed, which likely corresponded with fracture in the opposing cortex for intact femurs or a secondary fracture site for treated defects. For defects treated with gyroid scaffolds, failure occurred at the proximal interface in 39% (9/23 defects), the distal interface in 61% (14/23 defects), and away from the interface in 5% (1/23 defects). A summary of torsional results is shown in Fig. 5 and tabulated in S.I. Table 2. The average maximum torque and stiffness of the intact femur (0.38 N-m, 0.023 N-m/ $^\circ$ ) in this study are similar to previously reported by our group (Kolambkar et al., 2011). Empty defects showed minimal torsional resistance, further evidence that no bony bridging occurred. No significant difference in torsional strength nor stiffness was observed between empty and large pore implants. This was attributed to the observed misalignment of large pore implants. Due to the large pore size relative to the diameter and cortical wall thickness of the bone ends,



**Fig. 3.** Representative X-ray radiographs of femurs at 12-weeks for all groups. (A) Large pore scaffold, (B) small pore scaffold, (C) large pore scaffold + BMP2, (D) empty, (E) intact.

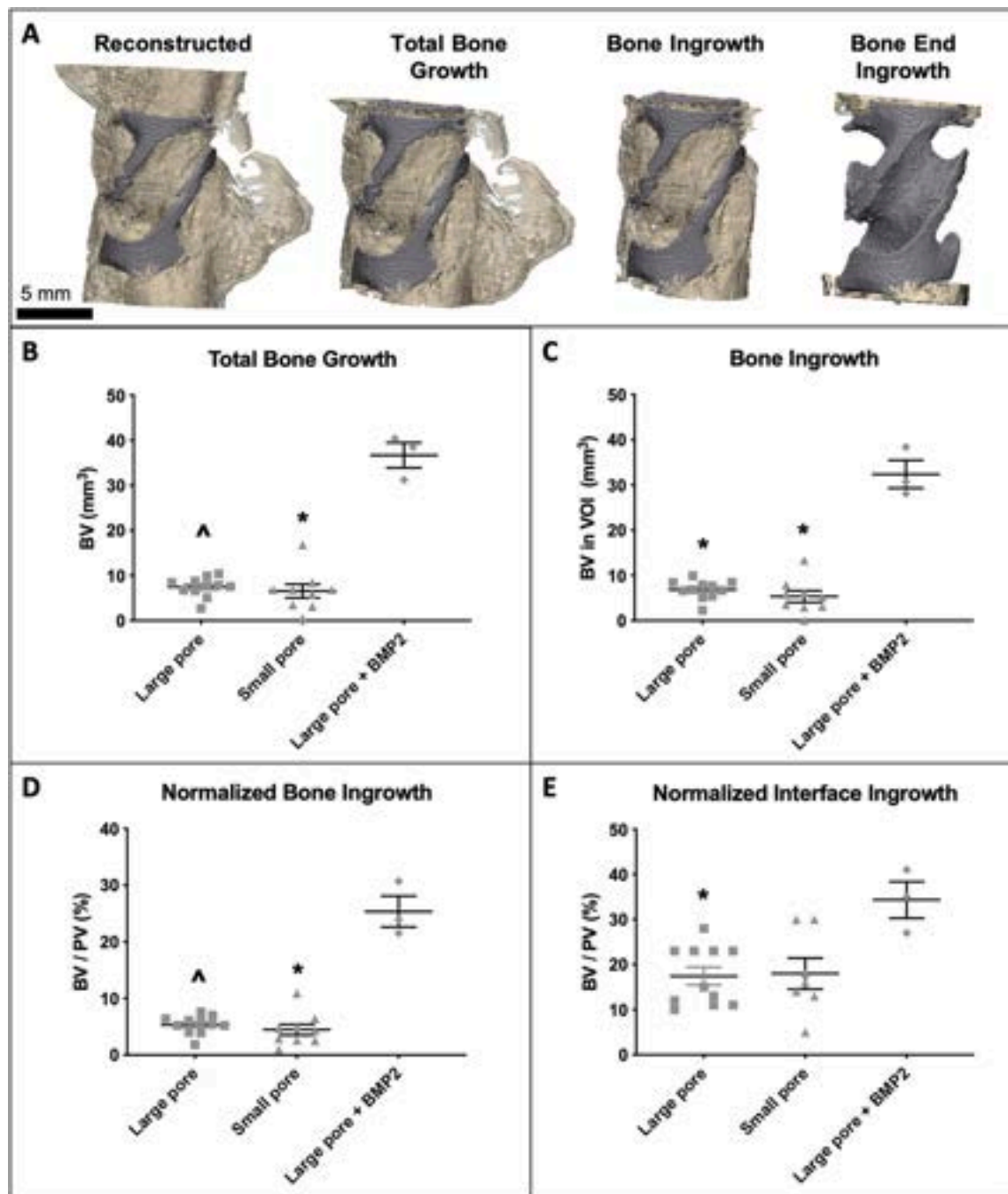


**Fig. 4.** Bone volume of explanted femurs assessed using  $\mu$ CT evaluation. (A) Representative bone volume reconstructions for the bone growth metrics evaluated. (B) Total bone growth volume, (C) Bone ingrowth volume within the defined VOI surrounding the implant, (D) Bone ingrowth normalized by the available pore volume. (E) Normalized interface ingrowth at the interface with lower bone volume. Bar represent mean and standard error of the mean. One-way ANOVA K-W test, Dunn's MC test, \* $p < 0.05$  and ^ $p < 0.1$  versus large pore + BMP2 group.

most of the large pore implants were initially or became misaligned with the cortex, and some portion of the solid surfaces of the implant at one or both ends was not in contact with the bone ends. However, the torque and stiffness increase seen with the addition of BMP2 to the large pore implant (0.41 N-m, 0.057 N-m/°) indicated that lack of interface integration, likely due to contributions of oversized topology, was overcome with delivery of an osteoinductive biologic. Small pore implants exhibited torsional strength and stiffness (0.14 N-m, 0.013 N-m/°) which were significantly greater than the empty defects but not significantly different than the intact femurs. This indicated that the small pore implants achieved higher functional integration of the bone ends,

likely due to the distribution of the contact area of the implant to the bone end, and possibly the pore size relative to the geometry of the bone ends themselves.

Torque and torsional stiffness of treated defects were shown to be linearly related ( $R^2 = 0.93$ , Fig. 6). Intact defects showed a higher strength to stiffness ratio and less correlation than the defects treated with scaffolds. The higher stiffness in the BMP2 group relative to the intact femur is likely due to the increased bone longitudinal growth outside the volume of interest defined directly around the defect, which would theoretically increase polar moment of inertia and thus the torsional resistance of the construct. Strong correlation between torque

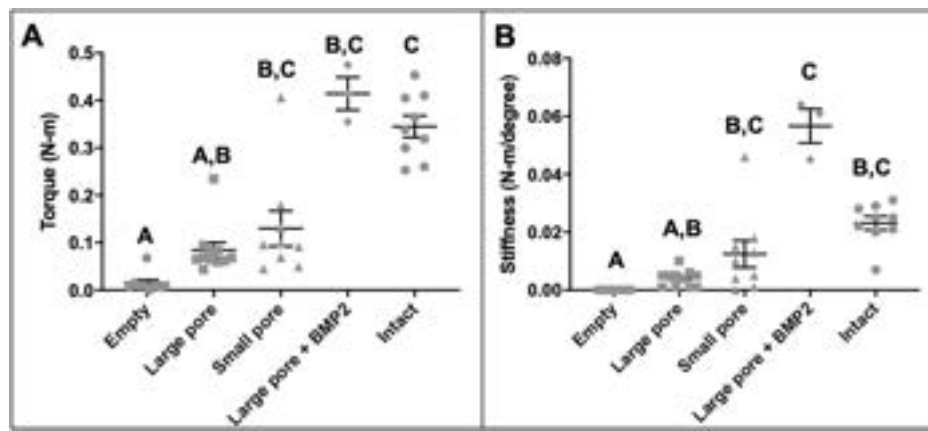


Fig. 5. Biomechanical evaluation of explanted femurs after 12-weeks. (A) Torsional strength and (B) torsional stiffness for all groups. Bar represent mean and standard error of the mean. One-way ANOVA K-W test, Dunn's MC test  $p < 0.05$ . Groups with shared letters are not significantly different.

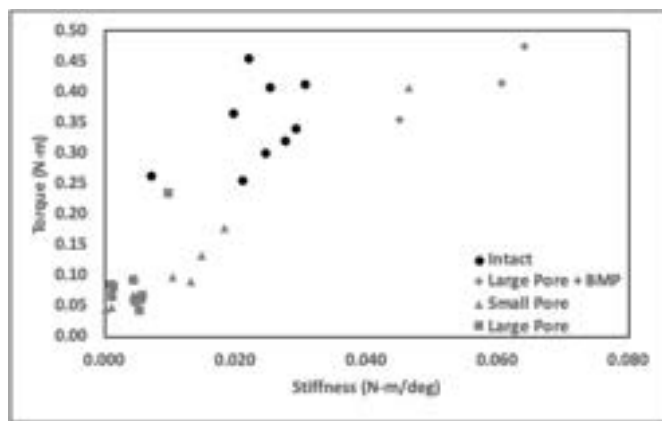


Fig. 6. Torque versus stiffness for intact femurs and treated defects.

and BV/PV was seen for defects treated with the large pore scaffolds with BMP and small pore scaffolds, but no positive correlation was seen for the empty large pore scaffolds (Fig. 7).

### 3.4. Histological evaluation

Histology of the explanted femurs allowed the examination of the bone ingrowth, enabling assessment of the tissue ingrowth within the scaffolds. Representative sections from large pore, small pore, and BMP-large pore implants are shown at low and high magnifications (Fig. 8). Overall, there was a lack of evidence of inflammation or adverse reaction to the scaffolds or the BMP2 alginate. In general, appositional bone growth on the scaffolds' surface was observed. As the surgical technique included a flat saw cut at the bone ends, the periosteum was activated and in many cases was observed to have begun to display penetrating ingrowth into and around the implant as seen in Fig. 8F. In the absence of bony fusion, fibrovascular tissue was seen within the porous structure.

The defects treated with BMP2 showed bone formation throughout the gyroid porous architecture, as well as longitudinal bone growth along the peripheral length of the VOI. In some defects, particularly in the large pore implant group, one end of the implant was clearly misaligned with the adjacent bone end, which is consistent with the  $\mu$ CT imaging and biomechanical results. In these cases, the misaligned end was encapsulated in muscle/fibrous tissue, but the opposite implant end integrated to the adjacent bone end.

## 4. Discussion

Bone is a geometrically complex network which undergoes constant remodeling driven by mechanical, chemical, and physical cues (Roddy et al., 2018; Zadpoor, 2015; Cowin, 2002, 2007). In the case of cortical bone defects, and ideal reconstructive scaffold should support load bearing and encourage bone bridging in a short period (Dimitriou et al., 2011). The present gyroid-sheet titanium alloy scaffolds, which have previously been shown to have high strength and fatigue resistance (Kelly et al., 2019a), were shown to support bone ingrowth to the implant ends allowing for recovery of mechanical strength by 12-weeks. The role of scaffold topology, surface topography, and delivery of osteoinductive factors in bone growth are discussed below.

### 4.1. Importance of bone-implant interface

In the present critically sized defect model, integration of the porous implant to the bone ends is imperative to achieve stability within the defect, thus allowing for ingrowth. Without ingrowth at both the proximal and distal bone-implant interfaces, the likelihood for displacement of the implant is high due to the critical size of the defect itself and the large implant length required to bridge it. In cases of a large gap or misalignment between the implant and one or both bone ends, the ability for ingrowth and recovery of mechanical strength is limited. Thus, the combined biomechanical, imaging, and histological analysis in this model is critical in assessing the relative performance of treatments to each other and the intact controls.

In the present study, there was a strong correlation between the measured maximum torque values and the bone ingrowth (BV/PV) into the scaffolds. Moreover, in defects where the normalized interface ingrowth differed by  $>2\%$  between the proximal and distal ends, the interface with less ingrowth was highly predictive of the failed interface during torsion testing (89% of defects). Fig. 9 shows an exemplary defect which fractured at the proximal interface. Prior to explanation, the implant was observed to be well aligned with the defect space. Following torsion, fracture was observed at the proximal interface, which was observed to contain a mixture of bone and fibrous tissue via histology.

After 12 weeks of implantation, gyroid-sheet scaffolds with BMP2 exhibited significant ingrowth at the interface and through the scaffold. Similarly, the small pore gyroid scaffolds exhibited considerable interface ingrowth which was not significantly different from those treated with BMP2. For both of these treatment groups, torsional strength and stiffness were not significantly different than the intact control. However, in the case of the large pore implant without BMP2, significantly lower bone ingrowth was observed at the interfaces and within the

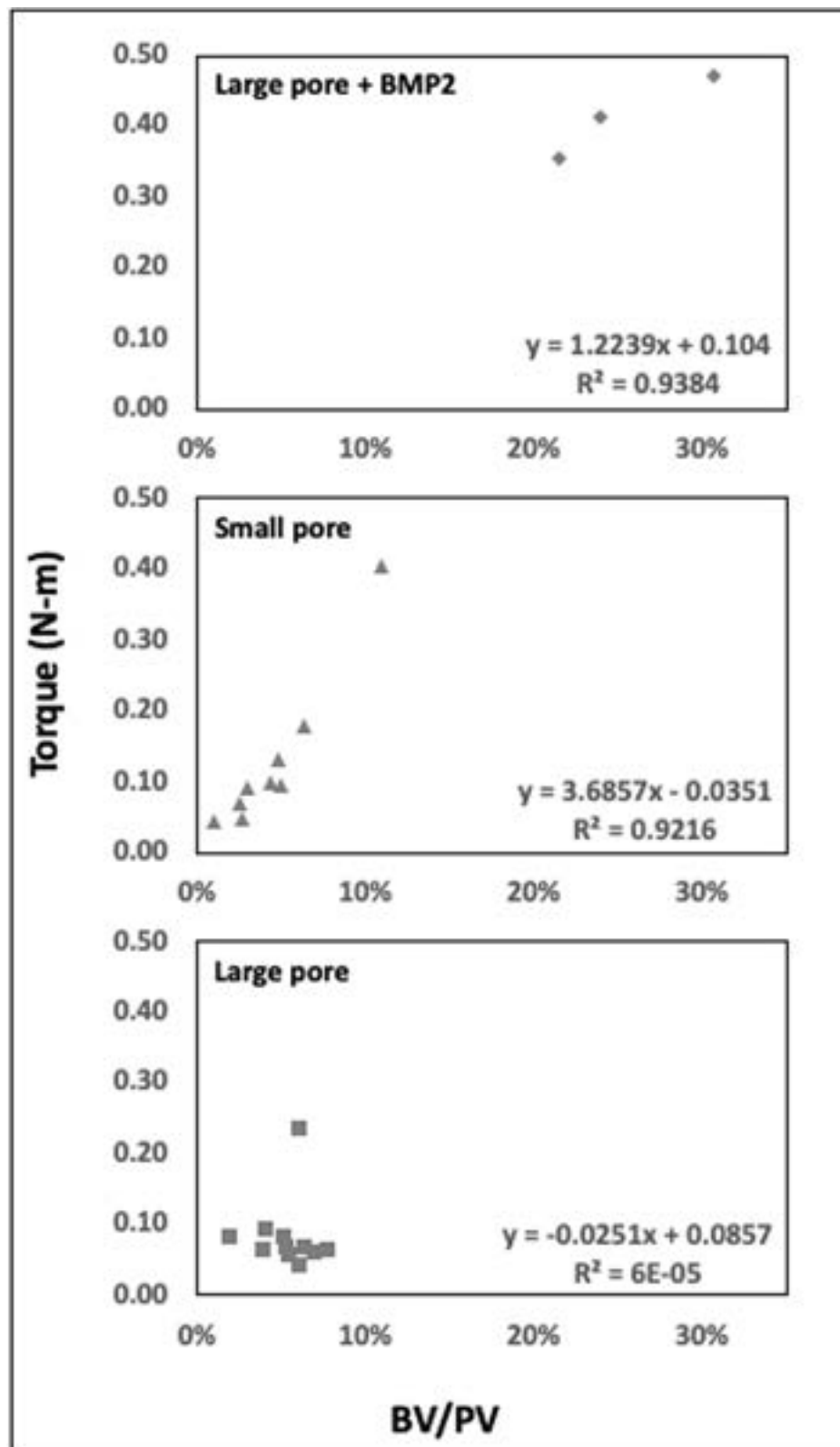
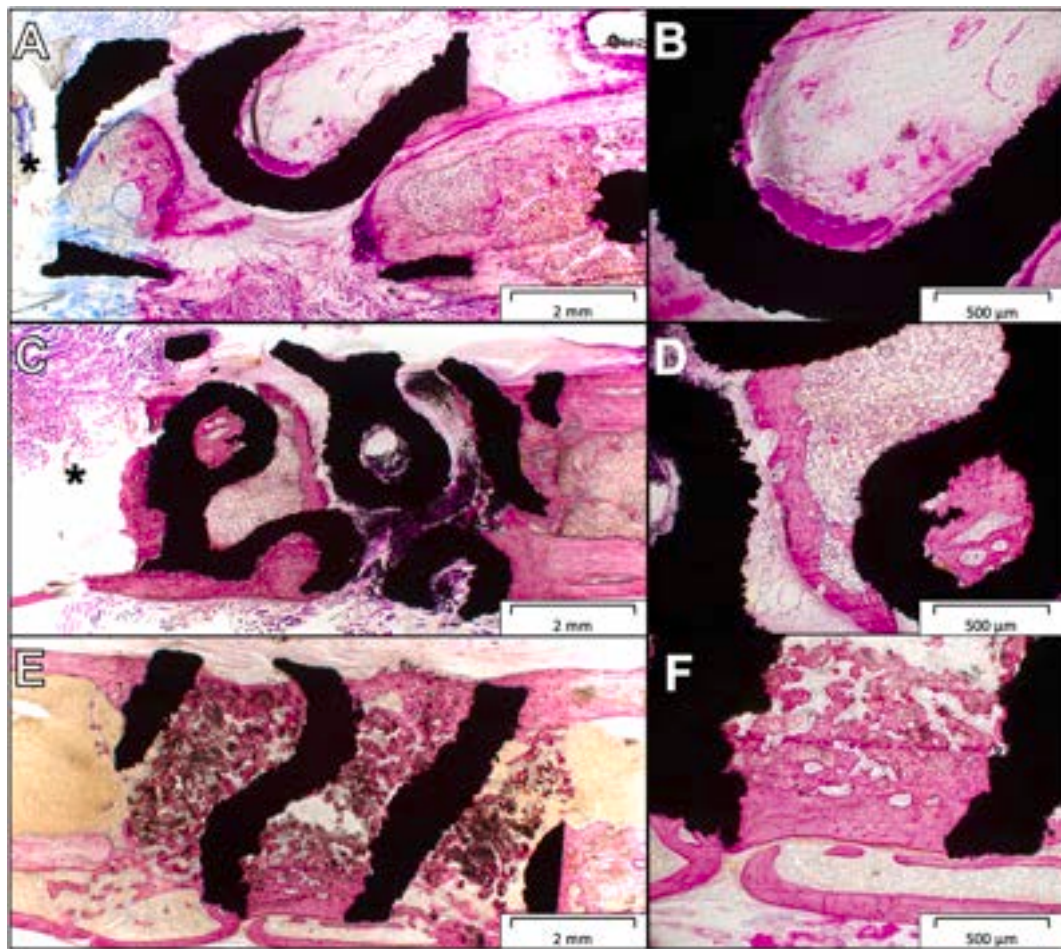


Fig. 7. Torque versus BV/PV for treated defect groups.

scaffold. In this group, torque values were significantly lower than the intact control, and review of the 12 week Faxitron images showed misalignment of the implant within the defect space or sizeable gaps between the bone end and implant. A discussion of the lack of alignment issues in the large pore scaffolds with BMP2 is discussed later.

The superior biomechanical performance and alignment of the empty small pore scaffolds relative to the larger pores could be attributed to increased surface area and more sites of ingrowth opportunity at the bone end interface. Interestingly, the diameter of the small pores in the present study are in fact larger than other similar porous scaffolds





**Fig. 8.** Histological evaluation of bone ingrowth at 12-weeks at (top) low magnifications with the proximal end up and (bottom) higher magnifications of each. (A, B) Large pore gyroid scaffold (C, D) Small pore gyroid scaffold, (E, F) Large pore gyroid scaffold with BMP. Black = implant (I), pink = bone (B), purple/blue = muscle and fibrous tissue (T). Asterisk indicates failed interface during torsion testing.

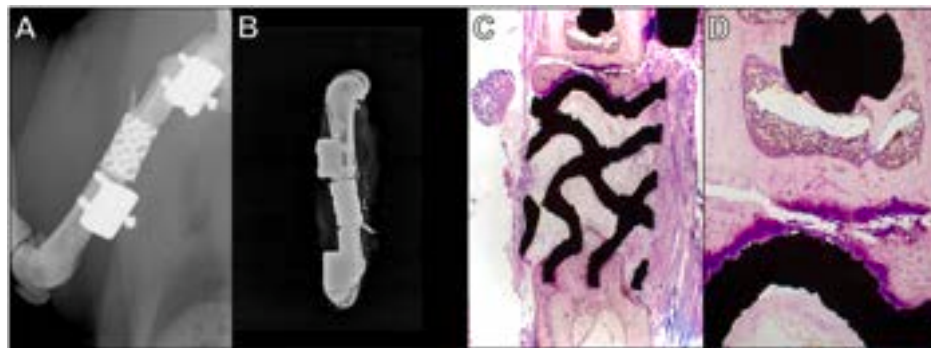


**Fig. 9.** Representative defect exhibiting failure at proximal interface. (A) In Vivo X-ray at 12-weeks (B) Lateral X-ray following torsion test, (C) Low Magnification histology showing failure at the interface. (D) High magnification histology showing separation occurred at the interface containing bone and fibrous tissue. Black = implant (I), pink = bone (B), purple/blue = muscle and fibrous tissue (T).

previously reported in similar rat models (van der Stok et al., 2013; Van der Stok et al., 2013). Conversely, the small pores in present scaffolds are smaller in diameter relative to those used in ovine segmental tibial defect models or those used clinically for reconstruction of large bone defects of the distal tibia (Dekker et al., 2018; Hamid et al., 2016; Anne-Marie Poblath et al., 2018). One of the limitations realized with the current rodent model is the relative size of the bone ends to the pores of the scaffold, which impaired the ability to fully assess functional performance of porous topologies with mesoscale pore sizes. The

promising results in the current study motivate the need for future large animal studies in which the anatomy is more closely matched to humans to better understand the role of scaffold topology and substrate curvature on repair of CSBDs.

#### 4.2. Role of implant surface

Direct apposition of bone to the surface without fibrotic encapsulation is imperative in achieving a stable interface between implant and

bone (van der Stok et al., 2013). The topography of the L-PBF titanium surface exhibits surface roughness ( $R_a \sim 7 \mu\text{m}$ ) which is on the micro-/nano scale that would be “noticed” by cells (Kelly et al., 2019b). Histological evaluation shows appositional bone formation on the surface of the titanium, both in the presence and absence of BMP (Fig. 8). It was qualitatively observed that bone formation was preferential to the concave surface of the implants, with marrow space encapsulated within the pore space in many cases (Fig. 8D). The higher surface area of the gyroid-sheet topology encourages high bone-implant contact and allows for subsequent ingrowth over the 12 weeks. Similar appositional bone formation to additively manufactured titanium alloy scaffolds has been observed in confined cortical defects in rabbits and sheep (Walsh et al., 2019; Cohen et al., 2017) and segmental defects in rodents (van der Stok et al., 2013). Thus, the surface topography of the present scaffolds is appropriate for treatment of critically sized bone defects.

Further the high surface area of sheet-based scaffolds presents an opportunity for further functionalization. Previous studies have investigated titanium scaffolds with surface coatings to promote healing, including calcium phosphate (CaP) and osteostatin coatings (Van Der Stok et al., 2015; Wieding et al., 2015). In both cases, the organic surface coatings were shown to promote osteoconduction. In the latter study, the initial release of the peptide improved bone volume versus an analogous but uncoated scaffold (Van Der Stok et al., 2015). In addition to improving osteoconduction, a further opportunity lies in surface coatings or functionalization for microbial resistance.

#### 4.3. Scaffold carrier for osteoinductive grafts

One of the benefits of meta-materials for use in biomedical applications in the design of porous networks which can be filled with bone graft or synthetic biologic materials. Due to the ability to maintain high strength while having significant void space, titanium scaffolds have been studied as composites with autograft, allograft, and other osteoinductive/osteoconductive materials to stimulate bone growth. Lindsey showed mesh-walled titanium cylinders filled with allograft resulted in 50% torsional stiffness of the intact contralateral canine femur at 12 weeks (Lindsey et al., 2006). Murakami also reported the increased performance of commercially pure titanium meshes impregnated with rhBMP2/PLA-PEG at varied doses of BMP2 to treat a segmental defect in the rabbit humeri (Murakami et al., 2002). The importance of dose and time of delivery of biologics has been demonstrated in preclinical models (van der Stok et al., 2013; Krishnan et al., 2017), and in clinical practice the ability to pack graft material into a porous implant and retain the graft at the defect site is critical to successful healing. The presently used alginate hydrogel system has been shown to have favorable release-kinetics, delivering a majority of the protein within the first 7 days, and sustaining continued release for up to 21 days (Kolambkar et al., 2011).

In the present study, large pore scaffolds achieved only 17% of intact stiffness, but when filled with BMP2, normalized stiffness increased to 244% of the intact controls. These results indicate that the role of the scaffold as a carrier of osteoinductive biologic is imperative to achieving fusion across the large defect. Because the large pore scaffolds with BMP did not show exhibit the same challenges with misalignment, it is concluded that early ingrowth induced by the BMP2 prevented expulsion of the implants from the defect. Prior to this study, the ability of the gyroid sheet titanium scaffold to retain a soft, non-structural BMP2 alginate hydrogel delivery system was unknown. Previous work from our group using the same rat model has demonstrated superior bone formation in defects treated with the alginate delivery system as compared to a collagen sponge. However, those defects were enclosed in a nanofiber mesh which physically retained the BMP2 at the defect site, but were unable to bear significant load (Krishnan et al., 2017). Present results showed continued bone growth observed via X-ray for all defects treated with BMP. Histology showed alginate material present throughout scaffold pores at the end point. Additionally, higher

torsional strength was observed for large pore titanium scaffolds with BMP2 relative to the previous nanofiber mesh study with the same dose of BMP2 (Kolambkar et al., 2011). These results are indicative that the BMP2 was locally retained within the highly porous scaffold and the composite construct with the titanium scaffold provided an improved functional environment.

A recent set of studies using AM titanium scaffolds with dodecahedron topology to treat 6 mm CSBD in rat femora have the most comparable model and biomechanical methods to the present study. Van der Stok demonstrated significantly higher bone ingrowth into dodecahedron titanium scaffolds at 12-weeks when filled with BMP2 in fibrin gel versus empty scaffolds (van der Stok et al., 2015). Defects treated with the BMP-fibrin gels exhibited an average torque twice that of the intact control, while the empty scaffold had only 53% the torsional strength of the intact femora. These trends are similar to present results in which defects treated with scaffolds with BMP2 delivered in alginate hydrogel and empty small pore scaffolds exhibited 120% and 38% of the maximum torque of the intact controls. In another study, osteostatin-coated titanium dodecahedron scaffolds were shown to improve osteoconductivity, increasing bone growth volumes and torsional strength compared to the bare scaffold control, but only achieved 66% of the torque of the intact femurs (Van Der Stok et al., 2015; van der Stok et al., 2015). The greater effect of the high strength titanium scaffold with gel-like carrier for biologics such as BMP2 is notable and reiterates the importance of a sustained release to the site to stimulate neo-bone formation. Future work will focus on more detailed studies of the release kinetics from such composite scaffolds. Additionally, extended time points in future work may help elucidate the effect of the high torsional stiffness.

## 5. Conclusion

In this study, high strength titanium scaffolds with a novel gyroid-sheet topology were produced via L-PBF and used to treat critically sized defects of the rat femora. The pore size of scaffolds relative to the bone end was shown to affect the stability of the construct and thus bone ingrowth and biomechanics at the implant-bone interface. In this case the small pore size proved more stable when used to reconstruct the defect without addition of osteoinductive factors. However, composite constructs with gyroid-sheet topology of large pores loaded with an alginate hydrogel carrying BMP2 demonstrated the highest bone ingrowth observed by  $\mu\text{CT}$ , and torsional strength and stiffness equivalent to the intact femur control. These results demonstrate functional and load bearing repair of segmental defects. Further work is needed to better understand the role of scaffold topology and curvature on bone growth, as well as optimization of dose and release of BMP2 from the scaffolds.

#### CRedit authorship contribution statement

**Cambre N. Kelly:** Conceptualization, Methodology, Investigation, Formal analysis, Writing - original draft. **Angela SP. Lin:** Investigation, Data curation, Writing - review & editing. **Kelly EH. Leguineche:** Investigation, Writing - review & editing. **Sudhanshu Shekhar:** Investigation, Writing - review & editing. **Robert E. Guldborg:** Conceptualization, Investigation, Writing - review & editing. **Ken Gall:** Conceptualization, Writing - review & editing.

#### Declaration of competing interest

The authors declare the following financial interests/personal relationships which may be considered as potential competing interests: C.N.K., R.E.G., and K.G. own stock/stock options in restor3d, Inc.

C.N.K., R.E.G., and K.G. own stock/stock options in restor3d, Inc. (Durham, NC).

## Appendix A. Supplementary data

Supplementary data to this article can be found online at <https://doi.org/10.1016/j.jmbbm.2021.104380>.

## References

- Al-Ketan, O., Rowshan, R., Abu Al-Rub, R.K., 2018. Topology-mechanical property relationship of 3D printed strut, skeletal, and sheet based periodic metallic cellular materials. *Additive Manufacturing* 19, 167–183.
- Anne-Marie Poblath, S.C., Razi, Hajar, Petersen, Ansgar, Weaver, James C., Schmidt-Bleek, Katharina, Windolf, Markus, Tatai, Andras Á., Roth, Claudia P., Schaser, Klaus-Dieter, Duda, Georg N., Schwabe, Philipp, 2018. Mechanobiologically optimized 3D titanium-mesh scaffolds enhance bone regeneration in critical segmental defects in sheep. *Sci. Transl. Med.*
- Bobbert, F.S.L., Lietaert, K., Eftekhari, A.A., Pouran, B., Ahmadi, S.M., Weinans, H., Zadpoor, A.A., 2017. Additively manufactured metallic porous biomaterials based on minimal surfaces: a unique combination of topological, mechanical, and mass transport properties. *Acta Biomater.* 53, 572–584.
- Cheng, A., Humayun, A., Cohen, D.J., Boyan, B.D., Schwartz, Z., 2014. Additively manufactured 3D porous Ti-6Al-4V constructs mimic trabecular bone structure and regulate osteoblast proliferation, differentiation and local factor production in a porosity and surface roughness dependent manner. *Biofabrication* 6 (4), 045007.
- Cheng, A., Cohen, D.J., Kahn, A., Clohessy, R.M., Sahingur, K., Newton, J.B., Hyzy, S.L., Boyan, B.D., Schwartz, Z., 2017. Laser sintered porous Ti-6Al-4V implants stimulate vertical bone growth. *Ann. Biomed. Eng.* 45 (8), 2025–2035.
- Cheng, A., Krishnan, L., Tran, L., Stevens, H.Y., Xia, B., Lee, N., Williams, J.K., Gibson, G., Guldberg, R.E., 2019. The effects of age and dose on gene expression and segmental bone defect repair after BMP-2 delivery. *JBMR Plus* 3 (2), e10068.
- Cohen, D.J., Cheng, A., Sahingur, K., Clohessy, R.M., Hopkins, L.B., Boyan, B.D., Schwartz, Z., 2017. Performance of laser sintered Ti-6Al-4V implants with bone-inspired porosity and micro/nanoscale surface roughness in the rabbit femur. *Biomed. Mater.* 12 (2), 025021.
- Cowin, S.C., 2002. Mechanosensation and fluid transport in living bone. *J. Musculoskelet. Neuronal Interact.* 2 (3), 256–260.
- Cowin, S.C., 2007. The significance of bone microstructure in mechanotransduction. *J. Biomech.* 40 (Suppl. 1), S105–S109.
- Dekker, T.J., Steele, J.R., Federer, A.E., Hamid, K.S., Adams Jr., S.B., 2018. Use of patient-specific 3D-printed titanium implants for complex foot and ankle limb salvage, deformity correction, and arthrodesis procedures. *Foot Ankle Int.* 1071100718770133.
- Dimitriou, R., Jones, E., McGonagle, D., Giannoudis, P.V., 2011. Bone regeneration: current concepts and future directions. *BMC Med.* 9, 66.
- Habibovic, P., de Groot, K., 2007. Osteoinductive biomaterials—properties and relevance in bone repair. *J. Tissue Eng Regen Med* 1 (1), 25–32.
- Hamid, K.S., Parekh, S.G., Adams, S.B., 2016. Salvage of severe foot and ankle trauma with a 3D printed scaffold. *Foot Ankle Int.* 37 (4), 433–439.
- Karcher, H., 1989. The triply periodic minimal surfaces of alan schoen and their constant mean curvature companions. *Manuscripta Math.* 64, 291–357.
- Kelly, C.N., Francovich, J., Julmi, S., Safranski, D., Guldberg, R.E., Maier, H.J., Gall, K., 2019a. Fatigue behavior of as-built selective laser melted titanium scaffolds with sheet-based gyroid microarchitecture for bone tissue engineering. *Acta Biomater.*
- Kelly, C.N., Evans, N.T., Irvin, C.W., Chapman, S.C., Gall, K., Safranski, D.L., 2019b. The effect of surface topography and porosity on the tensile fatigue of 3D printed Ti-6Al-4V fabricated by selective laser melting. *Mater. Sci. Eng. C* 98, 726–736.
- Kolambkar, Y.M., Dupont, K.M., Boerckel, J.D., Huebsch, N., Mooney, D.J., Huttmacher, D.W., Guldberg, R.E., 2011. An alginate-based hybrid system for growth factor delivery in the functional repair of large bone defects. *Biomaterials* 32 (1), 65–74.
- Krishnan, L., Priddy, L.B., Esancy, C., Klosterhoff, B.S., Stevens, H.Y., Tran, L., Guldberg, R.E., 2017. Delivery vehicle effects on bone regeneration and heterotopic ossification induced by high dose BMP-2. *Acta Biomater.* 49, 101–112.
- Li, G., Wang, L., Pan, W., Yang, F., Jiang, W., Wu, X., Kong, X., Dai, K., Hao, Y., 2016. In vitro and in vivo study of additive manufactured porous Ti6Al4V scaffolds for repairing bone defects. *Sci. Rep.* 6, 34072.
- Li, L., Shi, J., Zhang, K., Yang, L., Yu, F., Zhu, L., Liang, H., Wang, X., Jiang, Q., 2019. Early osteointegration evaluation of porous Ti6Al4V scaffolds designed based on triply periodic minimal surface models. *Journal of Orthopaedic Translation.*
- Lindsey, R.W., Gugala, Z., Milne, E., Sun, M., Gannon, F.H., Latta, L.L., 2006. The efficacy of cylindrical titanium mesh cage for the reconstruction of a critical-size canine segmental femoral diaphyseal defect. *J. Orthop. Res.* 24 (7), 1438–1453.
- Ma, S., Tang, Q., Feng, Q., Song, J., Han, X., Guo, F., 2019. Mechanical behaviours and mass transport properties of bone-mimicking scaffolds consisted of gyroid structures manufactured using selective laser melting. *Journal of the Mechanical Behavior of Biomedical Materials.*
- Mahmoud, D., Elbestawi, M.A., 2018. Selective laser melting of porosity graded lattice structures for bone implants. *Int. J. Adv. Manuf. Technol.*
- Murakami, N., Saito, N., Horiuchi, H., Okada, T., Nozaki, K., Takaoka, K., 2002. Repair of segmental defects in rabbit humeri with titanium fiber mesh cylinders containing recombinant human bone morphogenetic protein-2 (rhBMP-2) and a synthetic polymer. *J. Biomed. Mater. Res.* 62 (2), 169–174.
- Oest, M.E., Dupont, K.M., Kong, H.-J., Mooney, D.J., Guldberg, R.E., 2007. Quantitative assessment of scaffold and growth factor-mediated repair of critically sized bone defects. *J. Orthop. Res.* 25 (7), 941–950.
- Reichert, J.C., Saifzadeh, S., Wulschleger, M.E., Epari, D.R., Schutz, M.A., Duda, G.N., Schell, H., van Griensven, M., Redl, H., Huttmacher, D.W., 2009. The challenge of establishing preclinical models for segmental bone defect research. *Biomaterials* 30 (12), 2149–2163.
- Roddy, E., DeBaun, M.R., Daoud-Gray, A., Yang, Y.P., Gardner, M.J., 2018. Treatment of critical-sized bone defects: clinical and tissue engineering perspectives. *Eur. J. Orthop. Surg. Traumatol.* 28 (3), 351–362.
- Schemitsch, E.H., 2017. Size matters: defining critical in bone defect size! *J. Orthop. Trauma* 31 (Suppl. 5), S20–S22.
- van der Stok, J., Wang, H., Amin Yavari, S., Siebelt, M., Sandker, M., Waarsing, J.H., Verhaar, J.A., Jahr, H., Zadpoor, A.A., Leeuwenburgh, S.C., Weinans, H., 2013a. Enhanced bone regeneration of cortical segmental bone defects using porous titanium scaffolds incorporated with colloidal gelatin gels for time- and dose-controlled delivery of dual growth factors. *Tissue Eng.* 19 (23–24), 2605–2614.
- Van der Stok, J., Van der Jagt, O.P., Amin Yavari, S., De Haas, M.F., Waarsing, J.H., Jahr, H., Van Lieshout, E.M., Patka, P., Verhaar, J.A., Zadpoor, A.A., Weinans, H., 2013. Selective laser melting-produced porous titanium scaffolds regenerate bone in critical size cortical bone defects. *J. Orthop. Res.* 31 (5), 792–799.
- Van Der Stok, J., Lozano, D., Chai, Y.C., Amin Yavari, S., Bastidas Coral, A.P., Verhaar, J. A., Gómez-Barrera, E., Schrooten, J., Jahr, H., Zadpoor, A.A., 2015a. Osteostatin-coated porous titanium can improve early bone regeneration of cortical bone defects in rats. *Tissue Eng.* 21 (9–10), 1495–1506.
- van der Stok, J., Koolen, M.K., de Maat, M.P., Yavari, S.A., Alblas, J., Patka, P., Verhaar, J.A., van Lieshout, E.M., Zadpoor, A.A., Weinans, H., Jahr, H., 2015. Full regeneration of segmental bone defects using porous titanium implants loaded with BMP-2 containing fibrin gels. *Eur. Cell. Mater.* 29, 141–153 discussion 153-4.
- Wall, A., Board, T., 2014. The Compressive Behavior of Bone as a Two-phase Porous Structure. *Classic Papers in Orthopaedics*. Springer, pp. 457–460.
- Walsh, W.R., Pelletier, M.H., Wang, T., Lovric, V., Morberg, P., Mobbs, R.J., 2019. Does implantation site influence bone ingrowth into 3D-printed porous implants? *Spine J.*
- Wieding, J., Lindner, T., Bergschmidt, P., Bader, R., 2015. Biomechanical stability of novel mechanically adapted open-porous titanium scaffolds in metatarsal bone defects of sheep. *Biomaterials* 46, 35–47.
- Wilts, B.D., Apele Zubiri, B., Klatt, M.A., Butz, B., Fischer, M.G., Kelly, S.T., Spiecker, E., Steiner, U., Schroder-Turk, G.E., 2017. Butterfly gyroid nanostructures as a time-frozen glimpse of intracellular membrane development. *Sci Adv* 3 (4), e1603119.
- Yu, G., Li, Z., Li, S., Zhang, Q., Hua, Y., Liu, H., Zhao, X., Dhaidhai, D.T., Li, W., Wang, X., 2020. The select of internal architecture for porous Ti alloy scaffold: a compromise between mechanical properties and permeability. *Mater. Des.* 192, 108754.
- Yuan, H., Fernandes, H., Habibovic, P., de Boer, J., Barradas, A.M., de Ruiter, A., Walsh, W.R., van Blitterswijk, C.A., de Bruijn, J.D., 2010. Osteoinductive ceramics as a synthetic alternative to autologous bone grafting. *Proc. Natl. Acad. Sci. U. S. A.* 107 (31), 13614–13619.
- Zadpoor, A.A., 2015. Bone tissue regeneration: the role of scaffold geometry. *Biomater Sci* 3 (2), 231–245.
- Zadpoor, A.A., 2017. Mechanics of additively manufactured biomaterials. *J Mech Behav Biomed Mater* 70, 1–6.
- Zadpoor, A.A., 2018. Mechanical performance of additively manufactured meta-biomaterials. *Acta Biomater.*